Dynamic Modeling and Transient Performance Analysis of a LHP-MEMS Thermal Management System for Spacecraft Electronics

Yun-Ze Li, *Member, IEEE,* Yu-Ying Wang, and Kok-Meng Lee, *Fellow, IEEE*

***Abstract*—Transient performance analysis is essential for the successful design of a spacecraft thermal management system. This paper presents three dynamic models for analyzing system-level transient responses of a loop heat pipe (LHP)-micro-electromechanical-system (MEMS) thermal management system consisting of a LHP and a variable emittance radiator employing MEMS technologies. The recommended hybrid mathematical model, which is deduced from the fundamental 3-node and 4-node thermal networks, provides an efficient closed-form equation enabling direct calculation of the fluid mass flowrate in the LHP from the nodal temperatures of the thermal management system, and a set of state equations that independently compute the temperature responses of the cooled object, LHP evaporator, LHP condenser, and MEMS radiator. The temperature transients of a 50 W LHP-MEMS thermal management system, as well as the hydraulic responses inside the employed LHP, were numerically investigated and discussed in detail.**

***Index Terms*—Dynamic modeling, loop heat pipe, micro-electromechanical-system (MEMS) radiator, spacecraft electronics, thermal management, transient performance.**

NOMENCLATURE

A	Area of radiator's outer surface (m^2).
C_c	Thermal capacity of LHP condenser (J/K).
C_e	Thermal capacity of LHP evaporator (J/K).
$C_{\rm hp}$	Thermal capacity of entire LHP (J/K).
$C_{\rm ob}$	Thermal capacity of cooled object (J/K).
C_r	Thermal capacity of radiator (J/K).
$G_{\rm hp}$	Cycling mass flowrate of LHP working fluid (kg/m).
G_l	Mass flowrate inside LHP liquid line (kg/m).
G_v	Mass flowrate inside LHP vapor line (kg/m).
h_l	Specific enthalpy of liquid inside LHP (J/kg).
h_v	Specific enthalpy of vapor inside LHP(J/kg).
P_c	Working fluid pressure inside condenser (MPa).
P_e	Working fluid pressure inside evaporator (MPa).
$\Delta P_{\rm cap}$	Pressure head of evaporator's primary wick (MPa).
$Q_{\rm ex}$	Total external heat flux absorbed by the radiator (W).
Q_i	Exhaust heat of cooled object (cooling load) (W).
Q_r	Heat dissipated to the space by the radiator (W).
$R_{\rm cr}$	Thermal resistance between condenser and radiator (K/W).
$R_{\rm oc}$	Thermal resistance between cooled object and LHP condenser (K/W).
$R_{\rm oe}$	Thermal resistance between cooled object and LHP evaporator (K/W).
r_1–r_5	Elements of thermal connection matrix (W/K).
T_c	Absolute temperature of LHP condenser (K).
T_e	Absolute temperature of LHP evaporator (K).
$T_{\rm ob}$	Absolute temperature of cooled object (K).
T_r	Absolute temperature of radiator (K).
Z_l	Flow resistance of liquid line and wick (MPa·(kg/s)$^{-\beta}$).
Z_v	Flow resistance of LHP vapor line (MPa·s^2/kg^2).
Greek Symbols:	
β	Hydraulic modeling factor.
ε_e	Equivalent emittance of radiator.
$\varepsilon_{\rm hr}$	Emittance of high emittance radiator surface.
$\varepsilon_{\rm ll}$	Emittance of louver cells covering radiator.
φ_r	Exposing degree of MEMS radiator.
σ	Stefan-Boltzmann constant ($W/K^4 \cdot m^2$).
Subscrips:	
c	Condenser.
cap	Capillary.
e	Evaporator.
ex	External.
hr	High emittance radiator surface.
hp	Heat pipe.
l	Liquid.
ll	Low emittance louver cells.
ob	Cooled object.
r	Radiator.
v	Vapor.

Manuscript received September 8, 2009; revised January 10, 2010 and March 26, 2010. Date of publication August 16, 2010; date of current version October 1, 2010. This work was supported by the National Natural Science Foundation of China, under Grant 50506003, and the Aeronautic Science Foundation of China, under Grant 2008ZC51028. Recommended for publication by Associate Editor K. Ramakrishna upon evaluation of reviewers' comments.

Y.-Z. Li and Y.-Y. Wang are with the School of Aeronautic Science and Engineering, Beihang University, Beijing 100191, China (e-mail: liyunze@buaa.edu.cn; w.yy1986@163.com).

K.-M. Lee is with the Woodruff School of Mechanical Engineering, Georgia Institute of Technology, Atlanta, GA 30332 USA (e-mail: kok-meng.lee@me.gatech.edu).

Color versions of one or more of the figures in this paper are available online at http://ieeexplore.ieee.org.

Digital Object Identifier 10.1109/TCAPT.2010.2049358

I. INTRODUCTION

INTEGRATED with the newly emerged variable emittance radiator based on the micro-electromechanical-

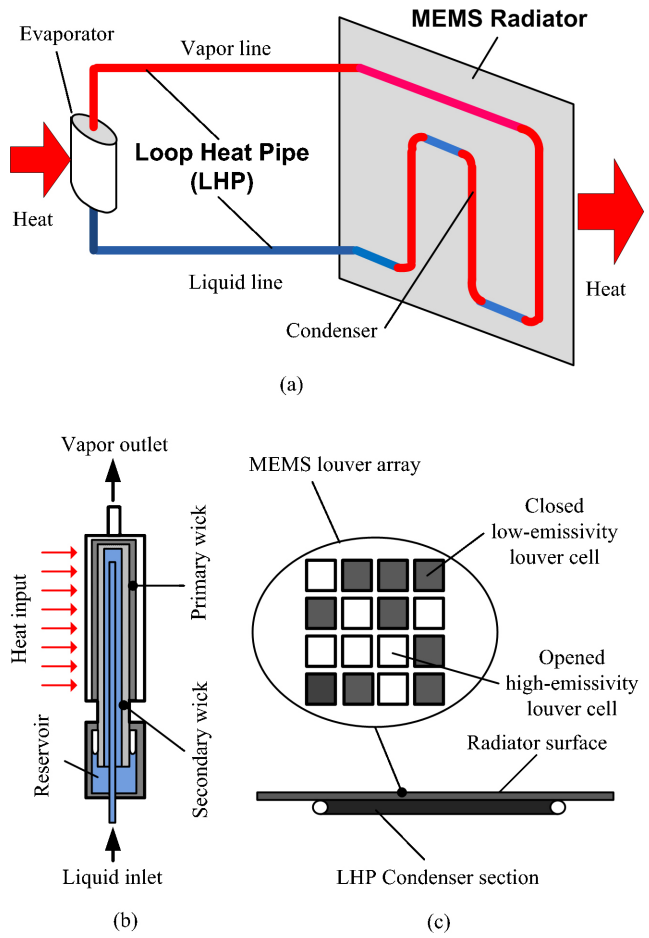

Fig. 1. LHP-MEMS thermal management system in space environment. (a) System schematic. (b) LHP evaporator. (c) MEMS radiator.

system (MEMS) technologies [1]–[3], the loop heat pipes (LHPs), which have been experimentally investigated as an effective two phase cooling technology for the highly compacted electronic components in high power density ground systems [4], [5], are considered to be a promising approach for active thermal management of advanced space missions like robotic spacecrafts [6], network missions on Mars [7], and the nano-satellites [8]. The centralized capillary structure inside a LHP evaporator can pump the working fluid to a condenser placed much further away than the heat transfer distance of a traditional heat pipe [9]–[11] by separating the vapor line from the liquid line. Although LHPs are usually treated as passive thermal control systems [6]–[8], the LHP-MEMS thermal management system considered here integrating a LHP and a MEMS variable emittance radiator can achieve highly accurate temperature control by active adjusting the heat radiation behavior at the outer surface of MEMS radiator [1]–[3], [8]. A concise dynamical model along with a systemic transient performance analysis is required for design optimization of a space LHP-MEMS thermal management system, especially when an immediate evaluation with numerical validation of its thermal control effects is necessary.

Significant effort has been made to understand the thermal and hydraulic characteristics of a LHP. The steady-state heat transfer behaviors of a 70 W miniature LHP were experimentally investigated in [12] with its starting-up transients and temperature oscillations under normal operating patterns. The transient heat and mass transfer performances in a cylindrical LHP evaporator were numerically investigated in [13]. A thermo-fluid dynamic model was proposed to determine the transient temperature distribution in the compensation chamber and the condenser section of a stainless steel/ammonia LHP in [14]. Mathematic models, which predict the transient thermal behaviors of the LHPs for aerospace applications, had been developed and validated independently with ground based experimental results in [15] and [16]. These numerical and experimental investigations on thermal and hydraulic performances of a LHP offer solid fundamentals for the dynamic modeling and transient performance analysis of our LHP-MEMS thermal management system.

This paper offers three different dynamic models for analyzing system-level transient performances of a LHP-MEMS thermal management system; 3-node and 4-node thermal network models, and a hybrid model of the two fundamental nodal networks. The hybrid mathematical model reveals the system-level temperature dynamics of the entire LHP-MEMS thermal management system, and the hydraulic responses inside the LHP. As will be shown, the hybrid model calculates the mass flow-rate of the LHP working fluid directly from the nodal temperatures which are state variables of the system, and therefore more concisely and more operable than the others. The temperature transients and hydraulic responses of a 50 W LHP-MEMS thermal management system are numerically investigated and discussed in detail.

II. System Description

Fig. 1(a) shows the LHP-MEMS thermal management system, where the LHP consists of an evaporator, two transport lines for vapor and liquid flow, respectively, and a tube-type condenser attached to the inner side of the MEMS variable emittance space radiator. The working fluid inside the LHP is ammonia. The detailed geometric and material characteristics of the employed LHP and MEMS radiator are provided in Table A1 in Appendix A.1.

The LHP-MEMS thermal management system is illustrated in Fig. 1(b). The exhaust heat of the cooled object is applied to the LHP evaporator, and transferred by conduction through the evaporator structure to vaporize the liquid ammonia inside it. The generated vapor travels along the LHP vapor line to the condenser where the vapor is condensed as heat is rejected to the outer space by the MEMS radiator. The condensate enters the LHP liquid line and is pumped back to the evaporator by a primary wick (embedded inside the evaporator), which acts as a capillary pump to provide the major pressure head for the fluid flow. A small compensation chamber [denoted as "reservoir" in Fig. 1(b)] is connected to the main part of the evaporator by a secondary wick which provides the capillary path for the local fluid path communication.

Fig. 1(c) illustrates the structure of a MEMS variable emittance radiator, where the MEMS louver array is mounted on the high emittance radiator surface to control the leaving heat flux. Since there is no air outside the spacecraft, the cooling

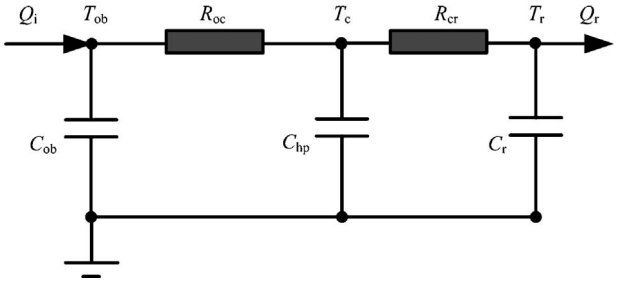

Fig. 2. 3-node thermal network model.

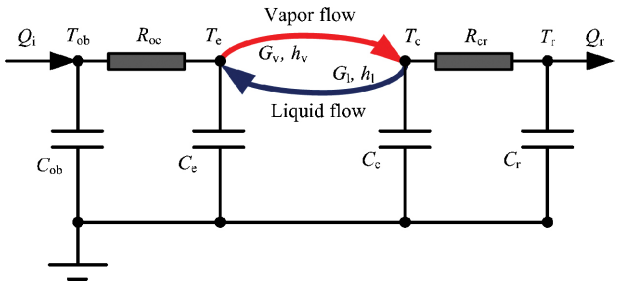

Fig. 3. 4-node thermal network model.

behavior of the radiator is dominated by heat radiation between the spacecraft and its orbit environment. When a louver cell in the MEMS array is opened, the high emittance radiator surface under it is exposed to the space environment; otherwise, the low emittance surface of the cover cell will face the space. Therefore, the cooling ability of the LHP-MEMS thermal management system can be adjusted by simply controlling the open number of louver cells in the MEMS array.

The net radiation heat flux leaving the MEMS radiator can be approximated by

$$Q_r = \varepsilon_e \sigma A T_r^4 - Q_{\text{ex}} \tag{1}$$

where the equivalent radiator emittance ε_e can be expressed as

$$\varepsilon_e = (\varepsilon_{\text{hr}} - \varepsilon_{\text{ll}})\,\varphi_r + \varepsilon_{\text{ll}} \tag{1a}$$

and the total external heat flux Q_{ex} absorbed by the radiator is contributed from the solar radiation, earth radiation, and earth reflection. In (1a), the exposing degree φ_r is a ratio of the exposed area (under the opened louver cells) to the total area of radiator surface. Since spacecrafts fly in the cold and vacuum space environment [17], thermal vacuum facilities [17], [18] or equivalent physical simulators [19] are required to simulate the space cooling behavior in (1) when performing a ground-based experiment. Additionally, the dynamic characteristics of the employed space simulator must be specially considered if a transient performance test is desired [19]. For these reasons, this paper focuses on modeling the transient behaviors for numerical investigations of a LHP-MEMS system.

III. Dynamic Modeling

A. 3-Nodal Thermal Network Model

Fig. 2 shows the 3-node thermal network representation for predicting the dynamics of a LHP-MEMS thermal control system. This network models the cooled object, LHP and radiator as three lumped thermal capacitances (C_{ob}, C_{hp}, and C_r) at nodal temperatures, T_{ob}, T_c, and T_r, respectively. The LHP condenser temperature T_c is chosen here as the representative temperature of the entire LHP node since the thermal inertia of the condenser section is usually much larger than that of the evaporator as schematically illustrated in Fig. 1(a) showing a typical implementation.

The dynamic model of the LHP-MEMS thermal control system can then be derived from the 3-node network using the principle of energy conservation at each nodal temperature

$$\mathbf{C}_3 \begin{bmatrix} \dot{T}_{\text{ob}} \\ \dot{T}_c \\ \dot{T}_r \end{bmatrix} = \begin{bmatrix} -R_{\text{oc}}^{-1} & R_{\text{oc}}^{-1} & \\ R_{\text{oc}}^{-1} & -(R_{\text{oc}}^{-1} + R_{\text{cr}}^{-1}) & R_{\text{cr}}^{-1} \\ & R_{\text{cr}}^{-1} & -R_{\text{cr}}^{-1} \end{bmatrix} \begin{bmatrix} T_{\text{ob}} \\ T_c \\ T_r \end{bmatrix} + \begin{bmatrix} Q_{\text{i}} \\ 0 \\ -Q_r \end{bmatrix} \tag{2}$$

where

$$\mathbf{C}_3 = \text{Diag}\begin{bmatrix} C_{\text{ob}} & C_{\text{hp}} & C_r \end{bmatrix}. \tag{2a}$$

In (2), the exhaust heat Q_i of the cooled object is also the heat load of the LHP-MEMS thermal control system and Q_r is the heat dissipated to the space by the radiator in (1).

Although the 3-node thermal network model (2) concisely expresses the temperature dynamics of LHP-MEMS thermal control system, it cannot predict the hydraulic responses within the LHP since no hydraulic calculation is involved in this 3-node model. Also, the fact that entire LHP is treated as a lumped-parameter node neglects the temperature difference between the evaporator and condenser (and thus its transient effects). These may lead to the propagation of modeling errors particularly if the values of the thermal capacitances and resistances between the lumped temperature nodes are not exact when solving for the solutions to (2).

B. 4-Nodal Thermal Network Model

The 4-node thermal network model takes into account the temperature difference between the evaporator and condenser by dividing the LHP into two different nodes; namely, the evaporator (with thermal capacity C_e) at T_e, and the condenser (with thermal capacity C_c) at T_c as shown in Fig. 3. Thus, this 4-node model provides an effective means to reveal the internal dynamics of the LHP as well as the temperature changes in the cooled object and in the MEMS radiator.

Similarly, the temperature dynamics can be derived using the principle of energy conservation from the 4-node network, which takes the form

$$\mathbf{C}_4 \begin{bmatrix} \dot{T}_{\text{ob}} \\ \dot{T}_e \\ \dot{T}_c \\ \dot{T}_r \end{bmatrix} = \begin{bmatrix} -R_{\text{oe}}^{-1} & R_{\text{oe}}^{-1} & & \\ R_{\text{oe}}^{-1} & -R_{\text{oe}}^{-1} & & \\ & & -R_{\text{cr}}^{-1} & R_{\text{cr}}^{-1} \\ & & R_{\text{cr}}^{-1} & -R_{\text{cr}}^{-1} \end{bmatrix} \begin{bmatrix} \dot{T}_{\text{ob}} \\ \dot{T}_e \\ \dot{T}_c \\ \dot{T}_r \end{bmatrix} + \mathbf{Q}_4 \tag{3}$$

where

$$\mathbf{C}_4 = \mathrm{Diag}\,[C_{\mathrm{ob}} \quad C_e \quad C_c \quad C_r] \tag{3a}$$

and

$$\mathbf{Q}_4 = [Q_i \quad G_l h_l - G_v h_v \quad G_v h_v - G_l h_l \quad -Q_r]^{\mathrm{T}}. \tag{3b}$$

In (3b), the specific enthalpies of the vapor and the liquid inside the LHP, h_v and h_l, can be, respectively, determined in terms of the evaporating and condensing temperatures by (4, 4a)

$$h_l = \mathrm{hlFun}(T_c) \quad \text{and} \quad h_v = \mathrm{hvFun}(T_e) \tag{4, 4a}$$

where hlFun() and hvfun() are the saturated enthalpy equations of the vapor and liquid ammonia given in Appendix A.2.

The mass flowrates (G_v and G_l of the vapor and liquid, respectively) inside a LHP, which depend on the pressure head of the capillary pump [the primary wick in Fig. 1(b)] and the flow resistances of the vapor line and the liquid line [Fig. 1(a)] [12]–[16], must be calculated in advance before (3) can be employed to analyze the temperature dynamics.

To facilitate the formulation of the hydraulic model, a general flow resistance Z is defined in

$$Z = \Delta P / G^{\beta} \tag{5}$$

where ΔP and G are the respective pressure drop across and mass flowrate through the flow element being considered (such as evaporator, and vapor or liquid line); and the hydraulic factor β has the value in the range of $1 \leq \beta \leq 2$. At typical LPH flow conditions, the value of β is about 2.0 for the vapor and liquid lines (based on fundamental theories of fluid mechanics), and 1.0 for the wick structures inside the evaporator based on the research findings [16]. Thus, the mass flowrate G_v in the LHP vapor line is given by

$$G_v = \sqrt{(P_e - P_c)/Z_v} \tag{6}$$

where the fluid pressures in the evaporator (P_e) and condenser (P_c) are functions of their respective nodal temperatures

$$P_e = \mathrm{pFun}(T_e) \quad \text{and} \quad P_c = \mathrm{pFun}(T_c). \tag{7, 7a}$$

The liquid mass flowrate in the LHP, which depends on the integrated flow resistance of the combined liquid line and evaporator, takes the form

$$G_l = \left\{ \left[\Delta P_{\mathrm{cap}} - (P_e - P_c) \right] / Z_l \right\}^{1/\beta_l} \tag{8}$$

where ΔP_{cap} is the pressure head of the primary wick (that acts as capillary pump enabling the flow of the working fluid); and the hydraulic modeling factor β_l for the integrated flow resistance has the value of 1 for the primary wick [16] and 2 for the liquid line.

Obviously, the 4-node thermal network model represented by (3)–(8) reflects changes in the mass flowrates of the working fluid and their influences on the nodal temperatures; thus, it provides more information than the 3-node network model (2) described in Section III-A. However, the 4-node thermal network demands much more complex calculations because the hydraulic parameters (ΔP_{cap}, Z_1, and β_1) determining the mass flowrates of the LHP working fluid in (6)–(8) are highly dependent on the evaporator geometry and the wick material inside it. The exact values of the evaporator parameters as well as the physical properties of the wick are usually very difficult to obtain without experiments. For these reasons, it is desired to derive a practical algorithm to calculate the mass flowrate, which will be developed in the next subsection.

C. Hybrid Dynamic Model and Algorithm

To inherit the advantages of the 3-node and 4-node thermal networks described in Sections III-A and III-B, respectively, while avoiding their disadvantages to the maximum extent, a hybrid dynamic model is directly developed from the fundamental energy conservation equations of the 3-node and 4-node thermal network given in (2) and (3) which require no experimental validations. Only a reasonable assumption (justified in the following discussion) is made for the simplification of the LHP mass flowrate calculation.

1) *Immediate Mass Flowrate Algorithm:* Since the hydraulic parameters (ΔP_{cap}, Z_1, and β_1) are determined by the structure and materials of the LHP evaporator and liquid line, the responses of LHP mass flowrate G_l and G_v will be dominated by the transient temperatures (T_e and T_c) of the evaporator and condenser as suggested by the mass flowrate equations for the vapor and liquid in (6)–(8). This is also consistent with the research findings [15] that the fluid viscosity of a LHP is a function of current temperatures as well as all other fluid properties. Therefore, it is possible to compute the change in mass flowrate directly from the nodal temperature changes.

For the objective to determine the dynamic changes of the nodal temperatures, we assume that the mass flowrate of the liquid flow G_l and that of the vapor flow G_v inside the LHP approximately satisfy

$$G_l = G_v = G_{\mathrm{hp}} \tag{9}$$

where G_{hp} is the mass flowrate of the working fluid recycling in the LHP. The rationales validating this assumption are as follows: 1) the volume of LHP reservoir V_r is very small; 2) the temperature changes of the evaporator and condenser are very slow, and their settling times are usually much longer than several thousand seconds according to published experimental findings [15], [16]; and 3) the saturated liquid density variations with the temperature changes are also very small [20]. Compared with the recycling mass flowrate determined by the operating cooling ability, the mass flowrate imbalance caused by the temperature change is enough to be neglected as follows:

$$\frac{V_r \left(\mathrm{d}\rho_l / \mathrm{d}T_e\right) \left(\mathrm{d}T_e / \mathrm{d}\tau\right)}{G_{\mathrm{hp}}} = \frac{V_r (h_v - h_l)}{Q_i} \left(\frac{\mathrm{d}\rho_l}{\mathrm{d}T_e}\right) \left(\frac{\mathrm{d}T_e}{\mathrm{d}\tau}\right) \ll 1. \tag{9a}$$

The LHP condenser temperature change can be determined from the energy conservation equation of the 3-node thermal

network in (2)

$$\dot{T}_c = \frac{1}{C_{\rm hp}}\left[\frac{T_{\rm ob}-T_c}{R_{\rm oc}} - \frac{T_c - T_r}{R_{\rm cr}}\right]. \tag{10}$$

Substituting (10) into the energy conservation equation (3) at the condenser node of the 4-nodal thermal network in Fig. 3 yields a closed form equation for calculating the mass flowrate $G_{\rm hp}$ of the working fluid from the nodal temperatures

$$G_{\rm hp} = \frac{1}{h_v - h_l}\left\{\frac{C_c}{C_{\rm hp}}\frac{(T_{\rm ob}-T_c)}{R_{\rm oc}} + \left(1-\frac{C_c}{C_{\rm hp}}\right)\frac{(T_c-T_r)}{R_{\rm cr}}\right\}. \tag{11}$$

The closed-form equation (11) offers a means much simpler than the traditional algorithm based on (6)–(8) to calculate the mass flowrate since only the thermal parameters (C_c, $C_{\rm hp}$, $R_{\rm cr}$, $R_{\rm oc}$, h_v, and h_l) that are also necessary for the temperature calculation (3) are required; this eliminates the needs to specify the hydraulic parameters (like $\Delta P_{\rm cap}$, Z_1, and β_1). Therefore, the computation of temperature changes requires less information on the LHP structure and material than the hydraulic parameter based approaches described in Section III-B.

2) *Hybrid State Equation for Temperature Changes:* The substitution of (11) into the energy conservation equation (3) at the LHP evaporator node of the 4-node thermal network yields the following state equation:

$$C_e\dot{T}_e = \frac{(T_{\rm ob}-T_e)}{R_{\rm oe}} - \frac{C_c}{C_{\rm hp}}\frac{(T_{\rm ob}-T_c)}{R_{\rm oc}} - \left(1-\frac{C_c}{C_{\rm hp}}\right)\frac{(T_c-T_r)}{R_{\rm cr}}. \tag{12}$$

Similar state equations can be derived at the nodes characterizing the temperatures of the cooled object and MEMS radiator. In summary, (10) and (12) and the energy conservation equations of the cooled object and MEMS radiator together can be written in a compact state-space form. The resulting hybrid state equation for the LHP-MEMS thermal management system is given in

$$C_{34}\begin{bmatrix}\dot{T}_{\rm ob}\\ \dot{T}_e\\ \dot{T}_c\\ \dot{T}_r\end{bmatrix} = \begin{bmatrix}-r_1 & r_1 & 0 & 0\\ r_1-r_2 & -r_1 & r_2-r_3 & r_3\\ r_4 & 0 & -r_4-r_5 & r_5\\ 0 & 0 & r_5 & -r_5\end{bmatrix}\begin{bmatrix}T_{\rm ob}\\ T_e\\ T_c\\ T_r\end{bmatrix} + \begin{bmatrix}Q_i\\ 0\\ 0\\ -Q_r\end{bmatrix} \tag{13}$$

where

$$\mathbf{C}_{34} = {\rm Diag}[C_{\rm ob} \quad C_e \quad C_{\rm hp} \quad C_r]. \tag{13a}$$

In (13), the elements r_i (where $i = 1, ..., 5$) of the thermal connection matrix are given in Table I.

Equations (11) and (13) together form the hybrid dynamical model, which has a concise form and is more practical than the 4-nodal thermal network model described by (3)–(8). It offers several advantages; it calculates both mass flowrate responses and temperature transients directly from the nodal temperatures; and it is more accurate and detailed than the 3-nodal model expressed by (2) which does not offer information on the mass flowrate.

TABLE I

ELEMENTS OF THE SYSTEM MATRIX $r_{\rm sys}$

Elements	Expressions	Elements	Expressions
r_1	$1/R_{\rm oe}$	r_4	$1/R_{\rm oc}$
r_2	$(C_c/C_{\rm hp})(1/R_{\rm oc})$	r_5	$1/R_{\rm cr}$
r_3	$(1-C_c/C_{\rm hp})(1/R_{\rm cr})$		

TABLE II

FUNDAMENTAL THERMAL PARAMETERS OF THE LHP-MEMS SYSTEM

Parameter (Unit)	Symbol	Value
Designed Operating Parameters		
Cooling ability of MEMS radiator (W)	Q_i	50
Cooled object temperature (K)	$T_{\rm ob}$	371.65
Radiator temperature (K)	T_r	308.15
LHP condenser temperature (K)	T_c	314.15
Thermal Network Parameters		
Thermal capacity of cooled object (J/K)	$C_{\rm ob}$	45.2
Thermal capacity of MEMS radiator (J/K)	C_r	135.6
Thermal capacity of evaporator (J/K)	C_e	35.2
Thermal capacity of condenser (J/K)	C_c	55.2
Thermal capacity of entire LHP (J/K)	$C_{\rm hp}$	90.4
Thermal resistance of LHP (K/W)	$R_{\rm hp}$	1.0
Thermal resistance between cooled object and LHP (K/W)	$R_{\rm oe}$	0.15
Thermal resistance between LHP and radiator (K/W)	$R_{\rm cr}$	0.12

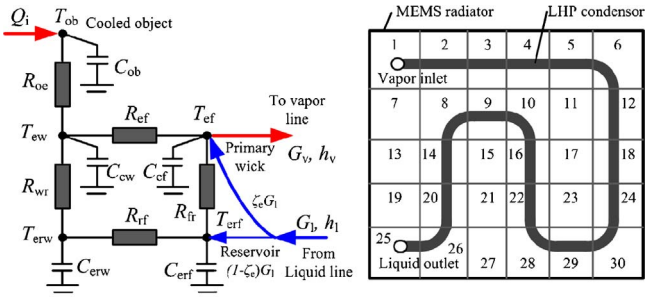

Fig. 4. Detailed model of LHP-MEMS thermal management system. (a) Evaporator-reservoir model. (b) Nodal layout of condenser-radiator assembly.

D. Validation of Hybrid Dynamic Model

The LHP-MEMS thermal management system of a 50 W micro satellite (Fig. 1) has been numerically analyzed using three different models. The results provide an effective means to evaluate the effectiveness of the hybrid dynamical model (Section III-C) against the traditional 4-nodal thermal network model (Section III-B), and a published model [15], [21] that has been experimentally validated. The values of the key parameters used in the simulation are summarized in Table II. Other detailed geometric and material characteristics are provided in Table A.1 of Appendix A.1.

To implement the published LHP model [15], [21] which serves as a basis for comparison, the evaporator of LHP is modeled using four temperature nodes [Fig. 4(a)]; the heated evaporator wall ($T_{\rm ew}$), fluid inside the heated evaporator section ($T_{\rm ef}$), the reservoir wall ($T_{\rm erw}$), and fluid inside the reservoir

(T_{erf}). The entire radiator is modeled using 30 elements as illustrated in Fig. 4(b) and with this nodal layout, the LHP condenser is divided into 21 temperature nodes. The cooled object is treated as one lumped temperature node. The equations for computing the nodal temperatures and the LHP mass flowrate can be found in [15] and [21], and are not repeated here.

As illustrated in Fig. 5(a), a cooling load cycle (50 W–25 W–35 W–50 W) is simulated for comparison. The initial cooling load (Q_i) is 50 W. The first cooling load change takes place at 100 s, then each cooling load remains unchanged for 3000 s. The temperature response of the cooled object (T_{ob}) is the prime interest of any thermal control systems and the simplified algorithm for LHP mass flowrate (G_{hp}) is fundamental to the recommended hybrid model in this paper, for these reasons the T_{ob} and G_{hp} profiles depicted in Fig. 5(b) and (c), respectively, are chosen here for discussion.

1) The T_{ob} responses calculated using the hybrid dynamical model (labeled as hybrid 3-4) agree well with those computed using the traditional 4-nodal thermal network model (4-nodal TNM) and detailed model [15], [21] in Fig. 4.
2) The largest differences of T_{ob} between the "hybrid 3-4" and "detailed model" are only 3.7% (10.9 K) at 50% designed cooling load, and this difference is further reduced to 1.6% (5.4 K) at 70% designed cooling load. The respective differences between "hybrid 3-4" and "4-nodal TNM" are even smaller; 1.9% (5.5 K) and 0.6% (1.9 K) at 50% and 70% designed cooling load, respectively.
3) The vapor mass flowrate (G_v) responds slightly faster than the liquid flowrate (G_l); however, the delay is very small. Since the mass flowrate curves of the "hybrid 3-4" and "detailed model" are almost the same, only the "detailed model" is plotted for a clear comparison against the cycling mass flow rate (G_{hp}) in the "hybrid 3-4" model. As shown in Fig. 5(c), the maximum steady state difference is about 3.2% in the simulated cooling load cycle.

The above findings conclude that the three models (hybrid dynamical model, traditional 4-nodal thermal network model, and the more detailed dynamical model [15], [21]) agree well. As a simplified practical algorithm, its accuracy is acceptable especially when dealing small or medium size disturbance.

IV. Numerical Investigation on Transient Performances

A. Simulation Cases and System Parameters

The thermal management system of a 50 W micro satellite is focused here, the layout and parameters of which have been detailed in Fig. 1 and Table II, respectively. The following three typical input changes with the cooled object of LHP and the MEMS radiator have been numerically investigated using the hybrid dynamic model proposed in this paper.

1) *Case I:* The exhaust heat Q_i of the cooled object is given a −10% step change.

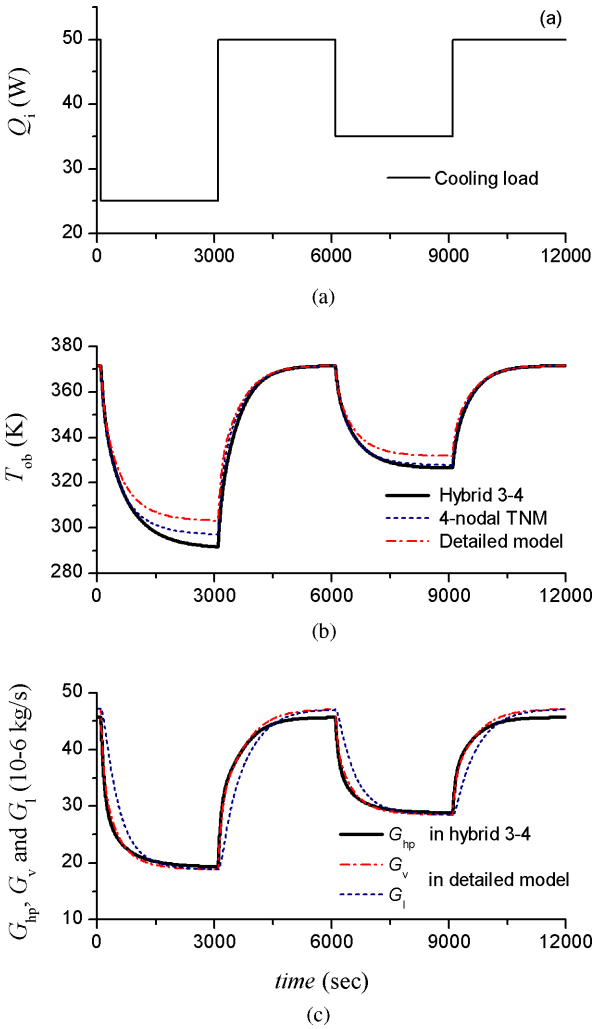

Fig. 5. Comparisons on numerical results. (a) Cooling load. (b) Temperature of the cooled object. (c) Mass flowrates.

2) *Case II:* The external heat load Q_{ex} of the radiator is subject to a step change from zero to +5% of the gross cooling ability of the radiator.
3) *Case III:* The exposing degree φ_r of the radiator is under a −10% step change of its initial value.

The above disturbances take effects at t = 100 s during simulation.

B. Results and Discussions

The numerical results are plotted in Figs. 6–8 in terms of 5% settling time τ (time required to reach within 5% of the final value) and the final output change rate ξ (the ratio between the final output change and the initial output) of each thermal and hydraulic output. These calculated results are listed in Table III.

Observations from these results are discussed as follows.

1) *Temperature Responses (Figs. 6 and 7, Table III):* Obvious differences between the temperature responses of the cooled object and the radiator can be seen in Fig. 6.

a) The radiator temperature T_r is more sensitive to the input changes which directly impact on the radiator (Q_{ex} and

TABLE III
PROPERTIES OF THE UNCONTROLLED SYSTEM TRANSIENTS

	Case I		Case II		Case III	
	τ (s)	ξ (%)	τ (s)	ξ (%)	τ (s)	ξ (%)
T_{ob}	1389	−3.9	1454	1.07	1518	2.2
T_r	1618	−2.6	1417	1.2	1451	2.62
T_e	1409	−3.7	1498	1.1	1511	2.3
T_c	1564	−2.7	1426	1.3	1468	2.60
P_c	1511	−21.6	1432	11.3	1499	24.7
G_{hp}	1206	−13.1	1453	1.77	1765	3.87

φ_r). The temperatures under Cases II and III increase directly to their final states (1.2% and 2.62% higher than their initial values) while the final changes with the temperature T_{ob} of the cooled object are only 1.07% and 2.2%, respectively, under these cases.

b) Both T_{ob} and T_r decrease directly to their new steady-state values under the Q_i change in Case I. However, T_{ob} is observed to settle down 1389 s later with a final drop of 3.9%. The final drop and settling time for T_r are 2.6% and 1618 s, respectively. These suggest that T_{ob} is more sensitive to the cooling load changes with Q_i than T_r.

c) The above temperature responses of changes T_{ob} and T_r are directly dominated by the external factors including cooling load change with Q_i under Case I, and cooling ability variations caused by Q_{ex} and φ_r under Cases II and III.

d) The temperature transients of the LHP evaporator and the LHP condenser (T_e and T_c in Fig. 7) are similar to that of the cooled object and the radiator, respectively (T_{ob} and T_r in Fig. 6), whereas the reasons are different.

e) Under the Q_i change in Case I, T_e decreases as the cooled object temperature T_{ob} (Fig. 6) decreases. T_c drops simultaneously since less ammonia was vaporized and flowed into the condenser with the reduced heat load. As compared with the T_{ob} transient under the same case, these dynamic processes are a little slower and less sensitive since the setting time and final change are 1409 s and −3.7% for T_e, 1564 s −2.7% for T_c, longer and smaller than that of T_{ob}.

f) Both T_e and T_c increase gradually as the radiator temperature T_r increases under Cases II and III since the corresponding Q_{ex} and φ_r changes result in decreasing the cooling ability of the radiator. T_c settles in 1426 s with final change of 1.3% under Case II while the respective values under Case III are 1468 s and 2.6%. The settling time and final changes of T_e are, respectively, longer and smaller than that of T_c under these two cases because T_c is more sensitive to the radiator side disturbances caused by Q_{ex} and φ_r.

g) The temperature trends of evaporator and condenser are determined by the heat transfer statuses between cooled object, LHP and radiator, as well as the mass flowrate changes of the working fluid inside LHP. The external disturbances (Q_i, Q_{ex}, and φ_r) can only result in the responses of T_e and T_c indirectly.

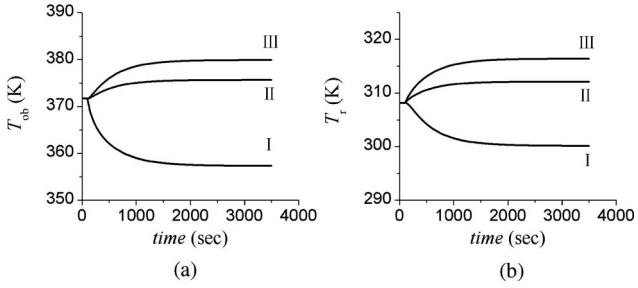

Fig. 6. Temperature responses of the cooled object and the radiator. (a) Cooled object. (b) Radiator.

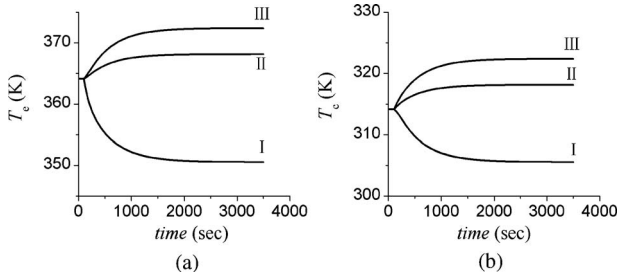

Fig. 7. Temperature responses of the LHP. (a) Evaporator. (b) Condenser.

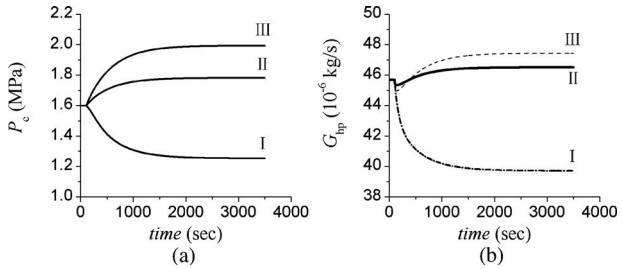

Fig. 8. Hydraulic responses inside the LHP. (a) Condensing pressure. (b) Mass flowrate.

2) *Hydraulic Responses of LHP (Fig. 8, Table III):* As compared with the transients of the condensing pressure, the working fluid mass flowrate inside the LHP responses more complexly under the different input changes in Cases I–III.

a) The condensing pressure P_c [Fig. 8(a)] responds to input changes most obviously among all the investigated outputs in Table III. It decreases gradually with the decrease of condenser temperature T_c [Fig. 7(b)] under Case I, and increases as T_c increases under the same conditions in Cases II and III. The final changes are −21%, 11.3%, and 24.7% of their respective initial steady-state values.

b) The mass flow rate G_{hp} [Fig. 8(b)] drops directly with a settling time of 1206 s and a final change rate of −13.1% in Case I. The reason is that less ammonia was vaporized with the reduced heat input at the LHP evaporator.

c) Beginning-stage temporary drops are found in G_{hp} before the final sustaining increases occurred under Cases II and III [Fig. 8(b)]. These temporary drops are because the increases of T_e are slower and smaller than that of T_c when Q_{ex} and φ_r suddenly changed as shown in Table III, The pressure deference between evaporator

and condenser is reduced according to (6). After these temporary drops, the transient values of $G_{\rm hp}$ increase gradually to their new steady-state points because the cooling load remained unchanged and a decreasing trend of enthalpy difference [$h_v - h_l$, in (11)] is caused by the increases of T_c. Therefore, larger mass flowrates of the working fluid are required at these situations. The final changes of $G_{\rm hp}$ under Cases II and III are 1.77% and 3.87%, respectively.

V. Conclusion

Three different dynamic models have been established for the transient performance analysis of the LHP-MEMS thermal management system. Among them, the hybrid dynamic model takes the advantages of calculating both of the temperature transients and the mass flowrate responses directly from the nodal temperature values; this makes the transient analysis of the LHP-MEMS thermal control system much easier and more convenient to be performed.

The numerical investigations on the typical input changes with the cooled object and with the MEMS radiator detected the transient characteristics on the temperature responses of LHP evaporator and condenser, as well as that of the cooled object and radiator. The numerical results also provide the argument that the transient changes with the condensing pressure and the mass flowrate of the LHP working fluid are the most obvious and the complex responses, respectively.

The model and results in this paper are expected to benefit the design, control, and analysis of thermal management systems for the advanced spacecrafts where space LHP-MEMS technologies are involved.

Appendix

A.1 Geometric Characteristics of LHP-MEMS System

The geometric and material characteristics of the focused LHP-MEMS system are listed in Table A1.

A.2 Properties of LHP Working Fluid

Temperature is the only variable which dominates the thermodynamic properties of statured working fluid inside the LHP. For the employed ammonia, a set of polynomial equations are fitted to determine the condensing pressure, the statured liquid enthalpy, and the statured vapor enthalpy from the original data of ammonia in [20].

The pressure of the statured ammonia is given by

$$\mathrm{pFun}(T) = W_0 + \sum_{i=i}^{5} W_i (T - 273.15)^i \qquad \text{(A.1)}$$

where W_i are the polynomial coefficients which values are given in Table A2. This statured pressure equation serves as the output equation of the dynamic models in (2), (3) and (13).

The enthalpy equations for the saturated liquid and vapor ammonia are provided by (A.2) and (A.3), respectively

$$\mathrm{hlFun}(T) = \left[X_0 + \sum_{i=i}^{5} X_i (T - 273.15)^i \right] \times 1000.0 \qquad \text{(A.2)}$$

TABLE A1
Geometric Characteristics of LHP-MEMS System

Components and Parameters	Values	Components and Parameters	Values
Evaporator		*Pipes and Condenser*	
Outer/inner diameter (mm)	20.0/17.0	Outer/inner diameter (mm)	5.0/3.0
Heated length (mm)	85	Liquid/vapor line length (mm)	950/800
Material	Stainless steel	Material	Stainless steel
Wick		*MEMS Radiator*	
Outer/inner diameter (mm)	17.0/8.0	Louver cell size (μm$\times\mu$m)	300×500
Mean pore radius (μm)	6.0	Louver number per square cm	400
Permeability (m^2)	10^{-13}	Louver coat	Gold
Porosity (%)	50	Louver base material	Silicon
Reservoir		Equivalent emittance range	0.1–0.9
Volume (cm^3)	18		

TABLE A2
Parameters of the Working Fluid Pressure Equation

Parameters	Values	Parameters	Values
W_0	4.293025E−1	W_3	1.558870E−6
W_1	1.605853E−2	W_4	2.940981E−9
W_2	2.351689E−4	W_5	1.322185E−12

TABLE A3
Parameters of the Saturated Liquid Enthalpy Equation

Parameters	Values	Parameters	Values
X_0	1.999759E+02	X_3	7.852176E−06
X_1	4.628426E+00	X_4	−6.695662E−08
X_2	3.406798E−03	X_5	2.181662E−09

$$\mathrm{hvFun}(T) = \left[Y_0 + \sum_{i=i}^{5} Y_i (T - 273.15)^i \right] \times 1000.0 \qquad \text{(A.3)}$$

where X_i and Y_i are the polynomial coefficients summarized in Tables A3 and A4, respectively. These two immediate equations are for the enthalpy calculation in (3) and (11). Note that the valid temperature ranges for the polynomials in (A.1) to (A.3) are 233.15 K $\leq T \leq$ 363.15 K.

A.3 Nodal Thermal Capacity Calculations

The thermal capacities of the cooled object and the radiator can be calculated by (A.4) and (A.5), respectively

$$C_{\rm ob} = m_{\rm ob} c_{\rm ob} \qquad \text{(A.4)}$$

$$C_r = m_r c_r \qquad \text{(A.5)}$$

where $m_{\rm ob}$ and $c_{\rm ob}$ are the mass and the average specific heat of the cooled object, respectively; m_r and c_r are the corresponding values for the MEMS radiator.

The thermal capacity for the entire LHP which employed in the 3-nodal thermal network model in Section III-A and

TABLE A4
PARAMETERS OF THE SATURATED VAPOR ENTHALPY EQUATION

Parameters	Values	Parameters	Values
Y_0	1.461799E+03	Y_3	−2.812115E−05
Y_1	1.065044E+00	Y_4	−7.197420E−08
Y_2	−7.765435E−03	Y_5	−1.777033E−09

our proposed hybrid dynamic model in Section III-C takes the form of

$$\begin{aligned} C_{\rm hp} &= m_{s,{\rm hp}}c_{s,{\rm hp}} + \frac{\mathrm{d}}{\mathrm{d}T}\left(m_{l,{\rm hp}}h_l\right) + \frac{\mathrm{d}}{\mathrm{d}T}\left(m_{v,{\rm hp}}h_v\right) \\ &= m_{s,{\rm hp}}c_{s,{\rm hp}} + m_{l,{\rm hp}}h_l\left(\frac{1}{h_l}\frac{\mathrm{d}h_l}{\mathrm{d}T} + \zeta_{\rm hp}\right) \end{aligned} \tag{A.6}$$

and

$$\zeta_{\rm hp} = \frac{1}{m_{l,{\rm hp}}}\cdot\frac{\mathrm{d}m_{l,{\rm hp}}}{\mathrm{d}T} + \frac{m_{v,{\rm hp}}}{m_{l,{\rm hp}}}\cdot\frac{1}{h_l}\cdot\frac{\mathrm{d}h_v}{\mathrm{d}T} + \frac{h_v}{h_l}\cdot\frac{1}{m_{l,{\rm hp}}}\cdot\frac{\mathrm{d}m_{v,{\rm hp}}}{\mathrm{d}T} \tag{A.7}$$

where $m_{\rm hp}$ and $c_{\rm hp}$ are the mass and the average specific heat of the entire LHP structure; $m_{l,{\rm hp}}$ and $m_{v,{\rm hp}}$ are liquid and vapor mass values inside LHP.

Similarly, the thermal capacities of the LHP evaporator and condenser can be expressed as (A.8) and (A.9), respectively

$$C_e = m_{s,e}c_{s,e} + m_{l,e}h_l\left(\frac{1}{h_l}\frac{\mathrm{d}h_l}{\mathrm{d}T} + \zeta_e\right) \tag{A.8}$$

$$C_c = m_{s,c}c_{s,c} + m_{l,c}h_l\left(\frac{1}{h_l}\frac{\mathrm{d}h_l}{\mathrm{d}T} + \frac{m_{v,c}}{m_{l,c}}\cdot\frac{1}{h_l}\cdot\frac{\mathrm{d}h_v}{\mathrm{d}T} + \zeta_c\right) \tag{A.9}$$

where

$$\zeta_e = \frac{1}{m_{l,e}}\cdot\frac{\mathrm{d}m_{l,e}}{\mathrm{d}T} + \frac{m_{v,e}}{m_{l,e}}\cdot\frac{1}{h_l}\cdot\frac{\mathrm{d}h_v}{\mathrm{d}T} + \frac{h_v}{h_l}\cdot\frac{1}{m_{l,e}}\cdot\frac{\mathrm{d}m_{v,e}}{\mathrm{d}T} \tag{A.10}$$

and

$$\zeta_c = \frac{1}{m_{l,c}}\cdot\frac{\mathrm{d}m_{l,c}}{\mathrm{d}T} + \frac{h_v}{h_l}\cdot\frac{1}{m_{l,c}}\cdot\frac{\mathrm{d}m_{v,c}}{\mathrm{d}T} \tag{A.11}$$

in which $m_{l,e}$ and $m_{v,e}$ are the liquid mass and vapor mass inside the evaporator; $m_{l,c}$ and $m_{v,c}$ are the respective values for the condenser; $m_{s,e}$ and $m_{s,c}$ are values of the structure mass for evaporator and condenser, and $c_{s,e}$ and $c_{s,c}$ are their specific heat values. The contributions of $\zeta_{\rm hp}$, ζ_e and ζ_c can be neglected when they are small enough.

ACKNOWLEDGMENT

The authors would like to thank Prof. J. Wang and Prof. Y.-H. Li for their support of this paper. They also appreciate the editors and reviewers for their constructive suggestions.

REFERENCES

[1] D. M. Douglas, J. Ku, L. Ottenstein, T. Swanson, S. Hess, and A. Darrin, "Effect of variable emittance coatings on the operation of a miniature loop heat pipe," *AIP Conf. Proc.*, vol. 746, no. 1, pp. 82–89, 2005.

[2] R. Osiander, S. L. Firebaugh, J. L. Champion, D. Farrar, and M. A. G. Darrin, "Microelectromechanical devices for satellite thermal control," *IEEE J. Sensors*, vol. 4, no. 4, pp. 525–531, Aug. 2004.

[3] D. Farrar, W. Schneider, R. Osiander, J. L. Champion, A. G. Darrin, and D. Douglas, "Controlling variable emittance (MEMS) coatings for space applications," in *Proc. 8th Intersociety Conf. Therm. Thermomech. Phenom. Electron. Syst.*, 2002, pp. 1020–1024.

[4] Y. F. Maydanik, S. V. Vershinin, M. A. Korukov, and J. M. Ochterbeck, "Miniature loop heat pipes a promising means for cooling electronics," *IEEE Trans. Compon. Packag. Technol.*, vol. 28, no. 2, pp. 290–296, Jun. 2005.

[5] R. Singh, A. Akbarzadeh, C. Dixon, M. Mochizuki, and R. R. Riehl, "Miniature loop heat pipe with flat evaporator for cooling computer CPU," *IEEE Trans. Compon. Packag. Technol.*, vol. 30, no. 1, pp. 42–49, Mar. 2007.

[6] T. D. Swanson and G. C. Biru, "NASA thermal control technologies for robotic spacecraft," *Appl. Therm. Eng.*, vol. 23, no. 9, pp. 1055–1065, Jun. 2003.

[7] R. Nadalini and F. Bodendieck, "The thermal control system for a network mission on Mars: The experience of the Netlander mission," *Acta Astronautica,* vol. 58, no. 11, pp. 564–575, Jun. 2006.

[8] G. Birur, "Advanced thermal control architecture for future spacecraft," presented at the 12th Ann. Spacecraft Thermal Control Technology Workshop, EI Segundo, CA, Feb. 28, 2001.

[9] Z. J. Zuo, M. T. North, and K. L. Wert, "High heat flux heat pipe mechanism for cooling of electronics," *IEEE Trans. Compon. Packag. Technol.*, vol. 24, no. 2, pp. 220–225, Jun. 2001.

[10] T. Nguyen, M. Mochizuki, K. Mashiko, Y. Saito, I. Sanciuc, and R. Boggs, "Advanced cooling system using miniature heat pipes in mobile PC," *IEEE Trans. Compon. Packag. Technol.*, vol. 23, no. 1, pp. 86–90, Mar. 2000.

[11] J. Legierski and B. Wiecek, "Steady state analysis of cooling electronic circuits using heat pipes," *IEEE Trans. Compon. Packag. Technol.*, vol. 24, no. 4, pp. 549–553, Dec. 2001.

[12] Y. Chen, M. Groll, R. Mertz, Y. F. Maydanik, and S. V. Vershinin, "Steady-state and transient performance of a miniature loop heat pipe," *Int. J. Therm. Sci.*, vol. 45, no. 11, pp. 1084–1090, Nov. 2006.

[13] K. N. Shukla, "Thermo-fluid dynamics of loop heat pipe operation," *Int. Commun. Heat Mass Transfer*, vol. 35, no. 8, pp. 916–920, Oct. 2008.

[14] M. A. Chernysheva and Y. F. Maydanik, "Numerical simulation of transient heat and mass transfer in a cylindrical evaporator of a loop heat pipe," *Int. J. Heat Mass Transfer*, vol. 51, nos. 17–18, pp. 4204–4215, Aug. 2008.

[15] V. V. Vlassov and R. R. Riehl, "Mathematical model of a loop heat pipe with cylindrical evaporator and integrated reservoir," *Appl. Therm. Eng.*, vol. 28, nos. 8–9, pp. 942–954. Jun. 2008.

[16] T. Kaya, R. Pérez, C. Gregori, and A. Torres, "Numerical simulation of transient operation of loop heat pipes," *Appl. Therm. Eng.*, vol. 28, nos. 8–9, pp. 967–974, Jun. 2008.

[17] D. G. Gilmore, *Spacecraft Thermal Control Handbook*, 2nd ed. El Segundo, CA: Aerospace Press, 2002, ch. 19.

[18] J. A. Rouse and R. L. Corinth, "Meeting today's requirements for large thermal vacuum test facilities," in *Proc. 14th Space Simulation Conf. Testing Permanent Presence Space*, 1986, pp. 112–130.

[19] Y.-Z. Li, K.-M. Lee, and J. Wang, "Analysis and control of equivalent physical simulator for nanosatellite space radiator," *IEEE/ASME Trans. Mechatron.*, vol. 15, no. 1, pp. 79–87, Feb. 2010.

[20] C.-B. Wei, S.-X. Lu, and Z.-Y. Zhou, *Practical Handbook of Refrigeration and Air-Conditioning Engineering*. Beijing, China: China Machine Press, 2006, pp. 31–32.

[21] V. V. Vlassov and R. R. Riehl, "Modeling of a loop heat pipe for ground and space conditions," in *Proc. 35th Int. Conf. Environ. Syst.*, 2005, no. 2005-01-2935.

Yun-Ze Li (M'09) received the B.S. degree in thermal and electrical engineering from the Northern China Institute of Water Conservancy and Electric Power, Zhengzhou, China, in 1996, the M.S. degree in thermal power engineering from Xi'an Jiaotong University, Xi'an, China, in 2000, and the Ph.D. degree in engineering thermal physics from Tsinghua University, Beijing, China, in 2002.

Since 2010, he has been a Professor with the School of Aeronautic Science and Engineering, Beihang University, Beijing. He was a Visiting Scholar with the Georgia Institute of Technology, Atlanta, in 2007, and with National Cheng-Kung University, Tainan, Taiwan, in 2008. His current major research interests include thermal control and energy management of aerospace systems.

Yu-Ying Wang received the B.S. degree in engineering mechanics from Zhengzhou University, Zhengzhou, China, in 2003. She is currently pursuing the Master's degree from the School of Aeronautic Science and Engineering, Beihang University, Beijing, China.

Since 2007, she has been a Research Assistant with the Active Thermal Control and Advanced Energy System Laboratory, Beihang University, Beijing, China. She has published two technical papers. Her major research interests include soft computing, intelligent control, and reliability analysis of the structure and thermal systems of advanced spacecraft.

Kok-Meng Lee (M'89–SM'02–F'05) received the B.S. degree from the State University of New York, Buffalo, in 1980, and the S.M. and Ph.D. degrees from the Massachusetts Institute of Technology, Cambridge, in 1982 and 1985, respectively.

Currently, he is a Professor with the Woodruff School of Mechanical Engineering, Georgia Institute of Technology, Atlanta. His current research interests include system dynamics/control, robotics, automation, and mechatronics.

Dr. Lee is a Fellow of the American Society of Mechanical Engineers. He has received the National Science Foundation Presidential Young Investigator, Sigma Xi Junior Faculty Research, International Hall of Fame New Technology, and Kayamori Best Paper Awards.